

Mass ejection from neutron star mergers: different components and expected radio signals

Kenta Hotokezaka* and Tsvi Piran

Racah Institute of Physics, The Hebrew University of Jerusalem, Jerusalem, 91904, Israel

8 January 2015

ABSTRACT

In addition to producing a strong gravitational signal, a short gamma-ray burst (GRB), and a compact remnant, neutron star mergers eject significant masses at significant kinetic energies. This mass ejection takes place via dynamical mass ejection and a GRB jet but other processes have also been suggested: a shock-breakout material, a cocoon resulting from the interaction of the jet with other ejecta, and viscous and neutrino driven winds from the central remnant or the accretion disk. The different components of the ejected masses include up to a few percent of a solar mass, some of which is ejected at relativistic velocities. The interaction of these ejecta with the surrounding interstellar medium will produce a long lasting radio flare, in a similar way to GRB afterglows or to radio supernovae. The relative strength of the different signals depends strongly on the viewing angle. An observer along the jet axis or close to it will detect a strong signal at a few dozen days from the radio afterglow (or the orphan radio afterglow) produced by the highly relativistic GRB jet. For a generic observer at larger viewing angles, the dynamical ejecta, whose contribution peaks a year or so after the event, will generally dominate. Depending on the observed frequency and the external density, other components may also give rise to a significant contribution. We also compare these estimates with the radio signature of the short GRB 130603B. The radio flare from the dynamical ejecta might be detectable with the EVLA and the LOFAR for the higher range of external densities $n \gtrsim 0.5\text{cm}^{-3}$.

Key words: gravitational waves—binaries:close—stars:neutron—gamma-ray burst:general

1 INTRODUCTION

A binary neutron star (ns^2) merger is one of the most promising targets of ground-based gravitational-wave (GW) interferometers, such as Advanced LIGO, Advanced Virgo, and KAGRA (The LIGO Scientific Collaboration 2014; Accadia et al. 2011; Aso et al. 2013). The expected event rate of ns^2 mergers is $0.4 - 400\text{ yr}^{-1}$ (Abadie et al. 2010). Most of these events will be just above or just below the detection threshold. Observations of an electromagnetic counterpart will confirm the validity of these GW signals, increasing significantly the potential detection rate and detection confidence (Kochanek & Piran 1993). In addition, an electromagnetic counterpart will enable the localization of the sources and the identification of their host galaxies and their redshifts, enhancing significantly the potential information from this event. Finally any electromagnetic counterpart will

provide invaluable information on the physics of the merger process.

The detection horizon distance will extend up to a few hundred Mpc. The size of the GW-sky localization error box will depend on the number of detectors used and between a few tens and thousands Milky-Way size galaxies will reside within this error box (see e.g., Nissanke et al. 2011; Fairhurst 2011). Follow-up observations will be a challenging task, even for a search limited to these galaxies. Clearly, a good understanding of the expected electromagnetic signals is essential to detect an electromagnetic counterpart (Metzger & Berger 2012; Nissanke et al. 2013; Kanner et al. 2013; Kasliwal & Nissanke 2014; Bartos et al. 2014).

Ns^2 mergers have been recognized as the possible progenitors of short gamma-ray bursts (GRBs) (Eichler et al. 1989; Nakar 2007) and short GRBs and their afterglows are one of the most attractive electromagnetic counterparts of GW events. However, GRBs and their early afterglows are believed to be highly beamed with a half-opening angle $\theta_j \approx 10^\circ$ (Fong et al. 2014). This results in about 5% prob-

* E-mail: kenta.hotokezaka@mail.huji.ac.il

Table 1. Summary of mass ejection in different forms.

	Mass [M_{\odot}]	Kinetic Energy E [erg]	Fiducial E [erg]	Average $\beta\Gamma$	Fiducial $\beta\Gamma$	Average Y_e	Reference
Dynamical ejecta ^a	$10^{-4} - 10^{-2}$	$10^{49} - 10^{51}$	$5 \cdot 10^{50}$	$0.1 - 0.3$	0.2	$0.01 - 0.4$	[1]
GRB jet	$\lesssim 10^{-8}$	$10^{47} - 10^{50.5}$	10^{48}	> 30	–	–	[2]
Cocoon	$10^{-6} - 10^{-4}$	$10^{47} - 10^{50.5}$	10^{48}	$0.2 - 10$	0.3	–	[3]
Shock breakout	$10^{-6} - 10^{-4}$	$10^{47} - 10^{49.5}$	$10^{48.5}$	1	1	–	[4]
Wind ^b	$10^{-4} - 5 \cdot 10^{-2}$	$10^{47} - 10^{50}$	10^{50}	$0.03 - 0.1$	0.07	$0.2 - 0.4$	[5]

References;

[1] Goriely et al. (2011); Korobkin et al. (2012); Hotokezaka et al. (2013); Bauswein et al. (2013); Rosswog (2013); Piran et al. (2013); Wanajo et al. (2014),

[2] Nakar (2007); Wanderman & Piran (2014),

[3] Nagakura et al. (2014); Murguia-Berthier et al. (2014),

[4] Kyutoku et al. (2014); Metzger et al. (2015),

[5] Dessart et al. (2009); Fernández & Metzger (2013); Metzger & Fernández (2014); Perego et al. (2014); Just et al. (2014); Fernández et al. (2015).

^a This component is composed by the tidal tail and shocked component. The main difference between them is the value of Y_e . The tidal component can have a lower Y_e .

^b This component includes two cases depending on whether the remnant is a black hole or a neutron star. In the former the wind is just from the surrounding disk while in the latter it arises from the neutron star as well. The wind from the remnant neutron star has a higher value of $\beta\Gamma$ and Y_e . Note that the fiducial value used is an optimistic one.

ability¹ to detect a short GRB in coincidence with the GW signal (Schutz 2011; Nissanke et al. 2011; Seto 2015). Even if the viewing angle is larger than the jet opening angle, off-axis afterglows, called orphan afterglows, can be observed at late times when the relativistic jet slows down and its emission is less beamed. As the frequency of the peak flux of afterglows decreases with time, at sufficiently small viewing angles the off-axis afterglows in the optical to radio bands can be a good potential candidate of electromagnetic counterparts to GW events (van Eerten & MacFadyen 2011; Metzger & Berger 2012).

In addition to the GRB beamed emission and its late more isotropic orphan afterglow, electromagnetic waves will be emitted quasi isotropically at different stages from material that is ejected during the merger. Most notable one is a macronova (also called kilonova), an optical–infrared transient driven by the radioactive decay of the heavy nuclei synthesized in the ejecta (Li & Paczyński 1998; Metzger et al. 2010; Kasen et al. 2013; Barnes & Kasen 2013; Tanaka & Hotokezaka 2013; Grossman et al. 2014). Recently, the *Hubble Space Telescope* detected a near infrared bump at 9 days after the *Swift* short GRB 130603B (Tanvir et al. 2013; Berger et al. 2013), which is consistent with the theoretical expectation of macronovae. While the identification hinges on a single data point if correct this is the first observational evidence for a significant mass ejection with a high velocity from a ns² merger.

Synchrotron radiation of electrons accelerated in shocks formed between the (mildly) relativistic ejecta and the interstellar medium (ISM) is a second electromagnetic counterpart (Nakar & Piran 2011). This emission can last up to a few years and peaks in the radio band. All the ejected material will contribute to this emission, but different components with different velocities will contribute at different timescales, at different frequencies, and at different intensities. The rise time and the peak flux depend on the density

of the ISM surrounding the merger but for modest densities the radio signals can be observed up to the detector horizon (Piran et al. 2013).

Recent studies have shown that mass ejection from mergers is driven by several different processes. The most robust one, that appears in numerical merger simulations, is the dynamical mass ejection. If mergers are accompanied by GRBs then clearly relativistic GRB jets are another component. Other mass ejection mechanisms that have been proposed are merger shock-breakout material, viscous/neutrino/magnetically driven winds, and a possible cocoon that forms when the jet propagates within the other components of the ejecta.

The different components have different masses and kinetic energies. Their characteristics depend on the nature of the progenitors, in particular on their relative sizes, on the nature of the merger remnant, which could be either a black hole or a massive neutron star (MNS), as well on the, unknown yet, neutron star matter equation of state (see, e.g., Hotokezaka et al. 2013; Bauswein et al. 2013). The different components will interact with each other and these interactions will affect their dynamics (Bucciantini et al. 2012; Nagakura et al. 2014; Murguia-Berthier et al. 2014), possibly producing electromagnetic signatures (e.g., Bucciantini et al. 2012; Zhang 2013; Metzger & Piro 2014; Nakamura et al. 2014; Rezzolla & Kumar 2014; Cioffi & Siegel 2014; Kisaka et al. 2014).

In this paper we examine the long lasting radio emission arising from the different components of the ejecta. The structure of the paper is as follows: We summarize in Sec. 2 the properties of the different components of the ejecta. In Sec. 3 we calculate the expected long-lasting radio flares produced by the interaction of the different components of the ejecta with the ISM. In Sec. 4 we compare these estimates with the radio signature of the short GRB 130603B. Finally, in Sec. 5, we summarize our results and their possible implications on the detection of radio signals accompanying mergers.

¹ Note that these estimates take into account that the GW horizon is larger in the direction of the GRB hence the chance of coincidence with a short GRB is larger than the beaming fraction.

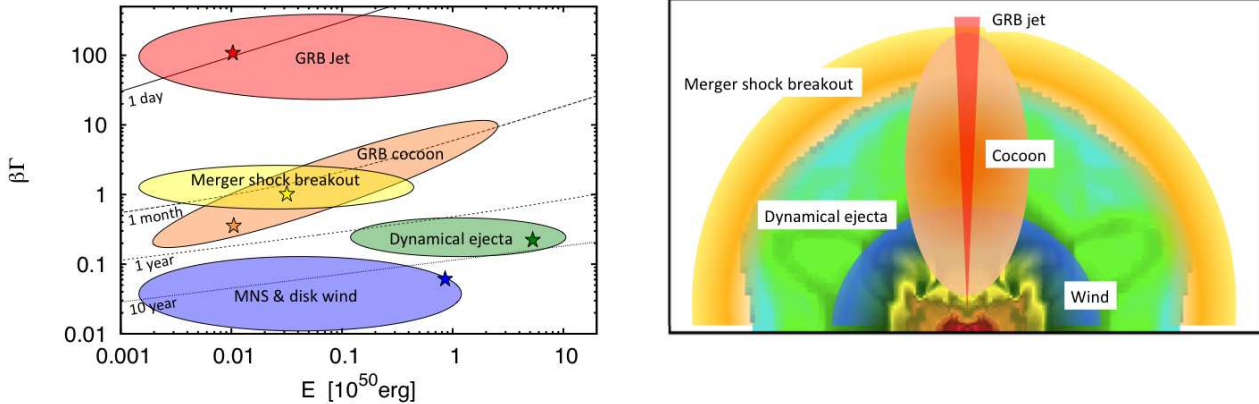


Figure 1. Left panel: the kinetic energy and the four-velocity of the different components of the ejecta. Also marked are the deceleration timescales of Eq. (2) assuming an external density of 1 cm^{-3} . The star in each component shows the fiducial model. Right panel: a schematic picture of the morphology of the different components of the ejecta on the meridional plane. The distribution of the dynamical ejecta is taken from a merger simulation (Hotokezaka et al. 2013). Other components are added schematically.

2 DIFFERENT COMPONENT OF EJECTA AND THEIR PROPERTIES

As material is ejected in different processes the different components will have different masses, kinetic energies, velocities, and electron fractions. The first three quantities determine the radio flare signals while all four are important for macronova estimate. Table 1 summarizes the values of these quantities as taken from the recent literature. The properties of the different components of the ejecta are also shown in Fig. 1. The left panel of the figure depicts the possible range of the kinetic energy, E , and the four velocity, $\Gamma\beta$. Here Γ is a Lorentz factor and β is a velocity in units of the speed of light c . Also shown in the figure are the deceleration timescales due to the interaction with the ISM, which are discussed later. This timescale gives the characteristic peak time of the radio flares from each component. The right panel of the figure shows schematically the expected morphology of the ejecta.

In the following, we briefly describe the properties of the different components. In each case we focus on the total mass, energy, and the corresponding velocities. We also mention the expected distribution of energy as a function of velocity, which is essential in order to estimate the radio flares from these components. For completeness we also mention the electron fraction Y_e . This is not needed for the radio estimate but it is a critical quantity that determines the composition of the ejected material as well as the heating rate that is essential for macronova estimates.

2.1 The dynamical ejecta

Gravitational and hydrodynamical interactions produce the dynamical ejecta. In many senses it is the easiest to calculate and as such it is the most robust element. It was investigated using Newtonian simulations (e.g., Davies et al. 1994; Ruffert et al. 1997; Rosswog et al. 1999; Rosswog 2013) and using general relativistic simulations (e.g., Oechslin et al. 2007; Hotokezaka et al. 2013; Bauswein et al. 2013). Ac-

cording to these numerical simulations, the mass and kinetic energy of the dynamical ejecta are expected to be in the range $10^{-4} \lesssim M_{\text{ej}} \lesssim 10^{-2} M_{\odot}$ and $10^{49} \lesssim E \lesssim 10^{51}$ erg, respectively. The median value of E in the general relativistic simulations is a few times 10^{50} erg. The properties of the dynamical ejecta are as follows.

The tidal ejecta. A fraction of the material obtains sufficient angular momentum and is ejected via tidal interaction due to non-axisymmetry of the gravitational forces. This matter is ejected even before the two stars collide with each other and it lasts as long as the gravitational field is not axisymmetric (about 10 ms after the merger in the case that the remnant is a MNS). This tidal component is mostly ejected into the equatorial plane of the binary within an angle about 20° (see e.g., Fig. 17 in Hotokezaka et al. 2013).

The electron fraction of the dynamical ejecta and the resulting nucleosynthesis have been studied in the literature (e.g. Goriely et al. 2011; Korobkin et al. 2012; Wanajo et al. 2014). The tidally ejected material has initially a low electron fraction $Y_e \ll 0.1$ as this matter does not suffer from shock heating and neutrino irradiation (Wanajo et al. 2014). This is particularly important concerning the possibility that this is the source of heavy (high atomic number) r -process nuclides, but it is not so relevant for our discussion that is concerned mostly with the radio flare. This fraction can increase by electron neutrino absorption or by positron absorption. The tidal component ejected at late times has higher Y_e values.

The shocked component. A shock is formed at the interface of the merging neutron stars. The shock sweeps up the material in the envelope of the merging neutron stars. Furthermore, a shock is continuously produced around the envelope of a remnant MNS as long as the MNS has radial oscillation. As a result, a fraction of the shocked material obtains sufficient energy and is ejected from the system. Recent general relativistic simulations show that this component can dominate over the tidal component in the case of a nearly equal mass binary (e.g., Hotokezaka et al. 2013; Bauswein et al. 2013). The shocked component is

ejected even in the direction of the rotation axis of the binary. The average electron fraction of the shocked components is relatively large compared with that of the tidal ejecta (Wanajo et al. 2014). It may be as large as $Y_e \sim 0.2 - 0.4$ and it will result in a different nucleosynthesis signature.

We take the velocity distribution of the dynamical ejecta from the result of a numerical relativity simulation of Hotokezaka et al. (2013) for a $1.4-1.4M_\odot$ ns² merger for the case of APR4 equation of state. The energy distribution of this model can be approximately described as $E(\geq \beta) \propto \beta^{-0.5}$ with a cut off at $\beta \simeq 0.4$ and an average velocity is $\beta \simeq 0.2$, where $E(\geq \beta)$ is the kinetic energy with a velocity larger than β . Note that it is not clear whether the cut off at $\beta \simeq 0.4$ is physical or that it arises just because it is difficult to resolve such a small amount of fast material in the numerical simulations. For our fiducial model, we use a total kinetic energy of 5×10^{50} erg.

The relativistic shock-breakout component. When the shock breaks out from the neutron star surface to the ISM, it is accelerated and a fraction of the shocked component can have a relativistic velocity with $\beta\Gamma \gtrsim 1$. Kyutoku et al. (2014) showed analytically that the kinetic energy of the relativistic ejecta can be $\sim 10^{47} - 10^{49.5}$ erg. More recently, Metzger et al. (2015) found that there is a mildly relativistic component with $\beta \gtrsim 0.8$ in a merger simulation of Bauswein et al. (2013). This fast component is likely resulted from the acceleration of a shock emerging from the neutron star surface. They found that the mass and kinetic energy of the fast component with $\beta \gtrsim 0.8$ are $\sim 10^{-5}M_\odot$ and $\sim 5 \times 10^{48}$ erg, respectively. Because of this large velocity, the radio signature of this component would be different from the slower material. We denote this component as a “shock-breakout material” and we consider it separately from the sub-relativistic dynamical ejecta.

Here, we assume that the kinetic energy distribution of this component is a simple power-law, $E(\geq \beta\Gamma) = 10^{48.5}(\beta\Gamma)^{-\alpha}$ erg as the fiducial model. The value of α varies from 1.1 for $\beta\Gamma \gg 1$ to 5.2 for $\beta\Gamma \ll 1$ (Kyutoku et al. 2014; Tan et al. 2001). We set α to be 3, which is valid around $\beta\Gamma \sim 1$ and we take into account only the fast component with $\beta\Gamma \geq 1$.

2.2 The ultra-relativistic jet

If ns² mergers are progenitors of short GRBs, they involve relativistic jets. Assuming the kinetic energy of the jet as the gamma-ray energy of the prompt emission, the energy of the jet can be estimated from the observed GRBs. The minimal and maximal values of the observed isotropic-equivalent gamma-ray energy for non-Collapsar short GRBs are 2×10^{49} erg and 4×10^{52} erg, respectively (Wanderman & Piran 2014). Taking into account the average value of the measured jet-half opening angles of $\theta_j \approx 10^\circ$ (Fong et al. 2014), the kinetic energy of a relativistic jet is in the range of $10^{47} - 3 \times 10^{50}$ erg. The luminosity function is rather steep and there are more weak GRBs than strong ones. Hence we consider here a fiducial GRB jet with a kinetic energy of 10^{48} erg and a jet-half opening angle of 10° .

2.3 The wind from the merger remnant

Some of the debris of the neutron stars form an accretion disk that surrounds the central remnant. The mass of this accretion disk is estimated to be in the range of $10^{-3} \lesssim M_{\text{disk}} \lesssim 0.3 M_\odot$ (see e.g., Shibata & Taniguchi 2006; Rezzolla et al. 2010; Hotokezaka et al. 2013). This accretion disk produces an outflow driven by viscous and neutrino heating. The properties of this outflow depend on the central object as follows.

A black hole with an accretion disk. The wind from an accretion disk surrounding a black hole has been explored, in the context of mergers, by Fernández & Metzger (2013); Just et al. (2014); Fernández et al. (2015). The disk is extremely dense and the accretion rate is huge. Initially it is opaque even for neutrinos. After $\sim 0.1 - 1$ s from the onset of the merger, the density and temperature of the accretion disk decrease and neutrino-cooling becomes inefficient. As a result, a fraction of the material is ejected isotropically due to the viscous heating in the accretion disk. The amount of ejected material is about 5 – 20% of the initial disk mass depending on the α -viscosity parameter and on the spin parameter of the black hole. Increasing these parameters, the fraction of the ejected mass to the initial disk mass increases. The average velocity of the ejecta is $0.03 \lesssim \beta \lesssim 0.05$ and the expected kinetic energy of the outflow is in the range of $10^{47} \lesssim E \lesssim 10^{50}$ erg. The average electron fraction is $Y_e \sim 0.2 - 0.3$.

A neutron star with an accretion disk. The wind from a neutron star with an accretion disk can be divided into three parts; a neutrino-driven wind from the remnant neutron star itself, a neutrino driven wind from the accretion disk, and a viscous driven wind from the accretion disk (Dessart et al. 2009; Metzger & Fernández 2014; Perego et al. 2014). The neutrino-driven wind expands into relatively high latitudes and it has a larger velocity $\beta \lesssim 0.1$ and a higher electron fraction $Y_e \sim 0.4$ than those of the viscous-driven wind. The amount of material ejected by the neutrino-driven wind depends on the lifetime of the central neutron star. Perego et al. (2014) showed that the ejected mass is more than $3 \times 10^{-3}M_\odot$ with a velocity $\beta \sim 0.06 - 0.9$ at 100 ms after the merger in the case of an initial disk mass of $0.17M_\odot$. Metzger & Fernández (2014) also showed that the amount of the ejected mass and average velocity are $M_{\text{ej}} \sim 10^{-3}M_\odot$ and $\beta \sim 0.05$ at 100 ms with an initial disk mass of $0.03M_\odot$. When a MNS does not collapse into a black hole, about 20% of the initial disk mass may be ejected as neutrino driven or viscous driven winds (Metzger & Fernández 2014).

In the following, we take the kinetic energy of 10^{50} erg with a single velocity $0.07c$ for the wind from the merger remnant as the fiducial model. Note that these values correspond to the most optimistic case. As shown later even in this case, the expected radio signals are very weak.

2.4 The cocoon

The interaction of a GRB jet with the pre-ejected material such as the dynamical ejecta or the wind along the rotation axis would produce a hot cocoon surrounding the jet (Nagakura et al. 2014; Murguia-Berthier et al. 2014; Rezzolla & Kumar 2014). After the jet emerges from the expanding ejecta, the cocoon will break out from the surface

of the ejecta and will expand nearly spherically. Assuming that the material inside the cone of a jet-half opening angle θ_j is shocked by the jet and forms a cocoon and the deposited energy into the cocoon is E_c , the Lorentz factor of the cocoon can be estimated as

$$\Gamma \approx 1 + 0.05 \left(\frac{M_{\text{ej}}(\theta_j)}{10^{-5} M_\odot} \right)^{-1} \left(\frac{E_c}{10^{48} \text{ erg}} \right), \quad (1)$$

where $M_{\text{ej}}(\theta_j)$ is the ejecta mass within θ_j . As the jet crossing time is comparable with the duration of a short GRB and the jet energy deposited in the cocoon will be comparable to the jet energy, we expect that the cocoon energy will be similar to the GRB jet energy. For our fiducial value, we take a kinetic energy of 10^{48} erg with a single velocity of $0.3c$ and the cocoon is sub-relativistic. Note that it becomes relativistic at energies higher than 10^{49} erg.

3 THE RADIO SIGNATURE

The various components of ejecta interact first with each other and ultimately with the ISM. This last interaction produces a long-lived blast wave. This shock that propagates into the ISM will enhance magnetic fields and accelerate electrons that will emit synchrotron radiation. The process is similar to GRB afterglows and to radio emission from some early supernova remnants. In this section, we explore the synchrotron radiation from a merger taking into account the various components of ejecta. Except for the relativistic jet we consider all components of the ejecta as spherically symmetric. We discuss the implications of this approximation in Sec. 3.3.

We assume that the ISM is homogeneous and characterized by an external density n . The ejecta slows down with the deceleration timescale given by

$$t_{\text{dec}} = \left(\frac{3E}{4\pi m_p c^5 n \Gamma_0 (\Gamma_0 - 1) \beta_0^3} \right)^{1/3}, \quad (2)$$

where Γ_0 and β_0 are the initial Lorentz factor and the corresponding initial velocity of the ejecta, m_p is the proton mass. The values of t_{dec} for the different components of ejecta are shown in the left panel of Fig. 1. For a mildly or sub-relativistic outflow the deceleration timescale characterizes the observed peak time. For an ultra-relativistic beamed jet with a viewing angle $\theta_{\text{obs}} > \theta_j$, we have an orphan afterglow. Namely, we do not see the highly beamed burst and early afterglow. But we see the late afterglow when it slows down and its less beamed emission includes our line of sight. As this happens when $\Gamma \sim \theta_{\text{obs}}^{-1}$, the peak time in the source frame is around t_{dec} given by Eq. (2) with $\Gamma \sim \theta_{\text{obs}}^{-1}$ instead of the initial Lorentz factor. Note that for a relativistic outflow the observer time is different from the time in source frame and it is smaller by a factor of Γ^{-2} . Note that for an observed GRB the peak in the radio arises when the observed frequency equals the typical synchrotron frequency.

The deceleration timescale (see the left panel of Fig. 1) suggests three types of the radio flares. First, the ultra-relativistic jet produces at early times the radio afterglow, that can be seen only by observers along the jet axis or close to it. Second, the mildly relativistic components, including the cocoon, the shock-breakout material, and the jet for an observer away from its axis produce radio flares with

a timescale of a few dozen days. Finally, the sub-relativistic dynamical ejecta produces a late-time radio flare with a timescale of a few years.

3.1 Ultra-relativistic beamed jet

The Blandford-McKee self-similar solution describes the jet dynamics, in the relativistic regime after the energy of the ISM swept up by the jet becomes comparable to the energy of the jet itself. Once the Lorentz factor of the jet decreases to $\Gamma \sim \theta_j^{-1}$, the jet expands laterally and approaches a quasi-spherical shape. To describe the evolution during this side-way expansion phase we adopt a semi-analytic formula for a homogeneous jet given by Granot & Piran (2012)², which shows a good agreement with the results of a numerical simulation by De Colle et al. (2012). The observed signal depends strongly on the viewing angle and we consider five different viewing angles $\theta_{\text{obs}} = (0^\circ, 30^\circ, 45^\circ, 60^\circ, 90^\circ)$.

To calculate the synchrotron radio emission we assume, as common in GRB afterglows and in radio supernovae modeling (see e.g., Sari et al. 1998), that the shock generates magnetic fields and accelerates electrons to a power law distribution $N(\gamma) \propto \gamma^{-p}$, where γ is the Lorentz factor of an accelerated electron. The value of p is estimated as $p \approx 2.1 - 2.5$ in late GRB afterglows and afterglows of low luminosity GRBs and as $p \approx 2.5 - 3$ in typical radio supernovae (Chevalier 1998). We assume $p = 2.5$. The total energy of the electrons and the magnetic field intensity are characterized by equipartition parameters: ϵ_e and ϵ_B that are the conversion efficiency from the internal energy of the shock into the energy of the accelerated electrons and magnetic fields, respectively. We set these parameters as $\epsilon_e = \epsilon_B = 0.1$. These values are consistent with those evaluated from late radio afterglows in long GRBs (Frail et al. 2000, 2005). For our purposes the radio emission is always below the cooling frequency hence the system has only two characteristic frequencies, the synchrotron frequency of the “typical” electron and the self absorption frequency. We implement the effect of the synchrotron-self absorption following Granot et al. (1999b); Rybicki & Lightman (1979). Once we determine the local emissivity we integrate over the intensity of each line of sight with an equal arrival time (see e.g., Sari 1998; Granot et al. 1999a)³.

3.2 Mildly and sub-relativistic isotropic components.

We briefly discuss the simple analytic estimates of the radio signals for a mildly and sub-relativistic ejecta (see Piran et al. 2013 for details). The hydrodynamics of a mildly and sub-relativistic blast wave with a kinetic energy E and an initial velocity β_0 expanding into a homogeneous ISM

² We adopt the conical model of Granot & Piran (2012). The difference of the afterglow flux between their different models is a factor $2 \sim 3$ during the side-expansion phase.

³ We do not use the afterglow library of van Eerten & MacFadyen (2011) which is incorrect below the absorption frequency. Above the absorption frequency our light curves are consistent with those of van Eerten & MacFadyen (2011).

with an external density n can be approximately described by $\beta = \beta_0$ until the deceleration time t_{dec} . The dynamics approaches to the Sedov-Taylor self-similar solution after t_{dec} .

The synchrotron emission is slow cooling and it is strongly suppressed by the self absorption below the self absorption frequency:

$$\nu_a(t) = \begin{cases} \nu_{a,\text{dec}} \left(\frac{t}{t_{\text{dec}}} \right)^{\frac{2}{p+4}} & (t \leq t_{\text{dec}}), \\ \nu_{a,\text{dec}} \left(\frac{t}{t_{\text{dec}}} \right)^{-\frac{3p-2}{p+4}} & (t > t_{\text{dec}}), \end{cases} \quad (3)$$

where

$$\nu_{a,\text{dec}} = 1 \text{ GHz} E_{49}^{\frac{2}{3(p+4)}} n^{\frac{3p+14}{6(p+4)}} \epsilon_{B,-1}^{\frac{2+p}{2(p+4)}} \epsilon_{e,-1}^{\frac{2(p-1)}{p+4}} \beta_0^{\frac{15p-10}{3(p+4)}}. \quad (4)$$

These expressions are valid for $\nu_a > \nu_m$, where ν_m is the synchrotron frequency of electrons with the minimum Lorentz factor. Here and elsewhere, Q_x denotes the value of $Q/10^x$ in cgs units.

For $\nu > \nu_a$, the peak flux and the peak time can be estimated as

$$F_{\text{peak}, \nu > \nu_a(t_{\text{dec}})} \approx 0.8 \text{ mJy} E_{49} n^{\frac{p+1}{4}} \epsilon_{B,-1}^{\frac{p+1}{4}} \epsilon_{e,-1}^{p-1} \beta_0^{\frac{5p-7}{2}} \times \left(\frac{D_L}{200 \text{ Mpc}} \right)^{-2} \left(\frac{\nu}{1.4 \text{ GHz}} \right)^{-\frac{p-1}{2}}, \quad (5)$$

and

$$t_{\nu > \nu_a(t_{\text{dec}})} = t_{\text{dec}} \approx 40 \text{ day} E_{49}^{\frac{1}{3}} n^{-\frac{1}{3}} \beta_0^{-\frac{5}{3}}, \quad (6)$$

where D_L is the luminosity distance to the source and we approximate the Lorentz factor as $\Gamma_0 - 1 \approx \beta_0^2$ in Eq. (6). The peak flux and its time depend sensitively on the external density, the kinetic energy, and the initial velocity of the ejecta in the optically thin regime.

For $\nu < \nu_a$ at t_{dec} , the peak flux and peak timescale are

$$F_{\text{peak}, \nu < \nu_a} \approx 0.1 \text{ mJy} E_{49}^{\frac{4}{5}} n^{\frac{1}{5}} \epsilon_{B,-1}^{\frac{1}{5}} \epsilon_{e,-1}^{\frac{3}{5}} \times \left(\frac{D_L}{200 \text{ Mpc}} \right)^{-2} \left(\frac{\nu}{150 \text{ MHz}} \right)^{\frac{6}{5}}, \quad (7)$$

and

$$t_{\nu < \nu_a(t_{\text{dec}})} \approx 200 \text{ day} E_{49}^{\frac{5}{11}} n^{\frac{7}{22}} \epsilon_{B,-1}^{\frac{9}{22}} \epsilon_{e,-1}^{\frac{6}{11}} \left(\frac{\nu}{150 \text{ MHz}} \right)^{\frac{13}{11}}. \quad (8)$$

In the optically thick regime, the peak flux and its timescale depend weakly on the external density and they are independent of the initial velocity of the ejecta. The dependence on the energy is also weaker than in the optically thin case.

As the velocity distribution is not uniform, we estimate the emission from each shell of matter and combined the results. For a given distribution of energies as a function of velocity, we divide the outflow into shells. An external ISM mass, $M(R)$, swept up at a radius R can be associated with each shell such that this mass slows down the shells:

$$M(R)(c\beta\Gamma)^2 = E(\geq \beta\Gamma). \quad (9)$$

Once we solve the implicit Eq. (9), we determine the observed light curves for each shell. We then combine the contributions of the different shells to obtain the total light curve. In the non-relativistic limit, the ejecta dynamics described by Eq. (9) is consistent with the self-similar solution derived by Chevalier (1982) up to a factor of order unity. In the relativistic limit and the case of $E(\geq \beta\Gamma) = \text{const}$, it

agrees with the Blandford-Mackee self-similar solution again up to a factor of order unity.

3.3 Numerical result

Figure 2 depicts the resulting radio light curves of the different components for our fiducial model (see Table 1 for the fiducial parameters). We examine three different values of the external density $n = 0.01 - 1 \text{ cm}^{-3}$ and we present the light curves for two observed frequencies 150 MHz (left panels) and 1.4 GHz (right panels) corresponding to the LOFAR and the EVLA of radio telescopes. We set the luminosity distance of the source to be 200 Mpc, which is roughly the sky averaged horizon distance of the advanced GW detectors for ns^2 mergers.

The ultra-relativistic jet always arrives first. This on-axis emission of the jet, the GRB radio afterglow, is the strongest at 1.4 GHz for low external densities $n \lesssim 0.1 \text{ cm}^{-3}$. At 150 MHz this GRB afterglow as well as the other relativistic component, the shock-breakout material, is strongly suppressed by self-absorption and it is much weaker. For a generic observer, the off-axis orphan afterglow at viewing angles of 60° and even at 45° is always subdominant compared to the shock-breakout material and the dynamical ejecta. The mildly relativistic component, that arises from the shock-breakout material, peaks later at around 20–100 days depending on the observed frequency and external density. Finally the sub-relativistic dynamical ejecta arises at late times (typically 1000 days). It is always the brightest at 150 MHz and it is also brightest at 1.4 GHz for higher external densities. For our fiducial parameters, that are based on a weak GRB, the radio emission from the sub-relativistic cocoon is always negligible.

As mentioned earlier, at early times, synchrotron self-absorption strongly suppresses the radio flux at 150 MHz. As a result, the peak flux is only $F_\nu \sim 0.01 \text{ mJy}$ for the relativistic components such as the shock-breakout material and the off-axis GRB jet for all the cases. As expected from Eq. (7), in this case the peak flux depends only on the kinetic energy among the parameters of ejecta. Indeed, the dynamical ejecta is the brightest as $F_\nu \sim 1 \text{ mJy}$ for $n \gtrsim 0.1 \text{ cm}^{-3}$ and its peak time is ~ 1000 days. For very low densities $n \lesssim 0.01 \text{ cm}^{-3}$, the on-axis GRB afterglow is comparable to the dynamical ejecta flare, peaking at about 20 days with $F_\nu \sim 0.1 \text{ mJy}$.

At 1.4 GHz, there are the early and late-time radio flares. The relativistic components such as the GRB afterglows and the shock-breakout material contribute the flare at early times as expected from Eqs. (5) and (6). For low densities $n \lesssim 0.1 \text{ cm}^{-3}$, the GRB afterglows within a viewing angle $\theta_{\text{obs}} \sim 30^\circ$ is the brightest at 1.4 GHz as $F_\nu \sim 0.1 - 0.5 \text{ mJy}$. Note that the off-axis GRB afterglows are very faint for large viewing angle $\theta_{\text{obs}} \gtrsim 60^\circ$ compared with the shock-breakout material and the dynamical ejecta. At this stage the originally beamed jet has already slowed down and its emission is already quasi spherical because of its low Lorentz factor (this is independent of the question how much did the jet physically expand sideways). As the jet energy is smaller than those of the other components, its radiation is weaker. The dynamical component dominates at late times $t \gtrsim 100$ days and has a relatively flat light curve.

As mentioned earlier, our fiducial GRB was a typical,

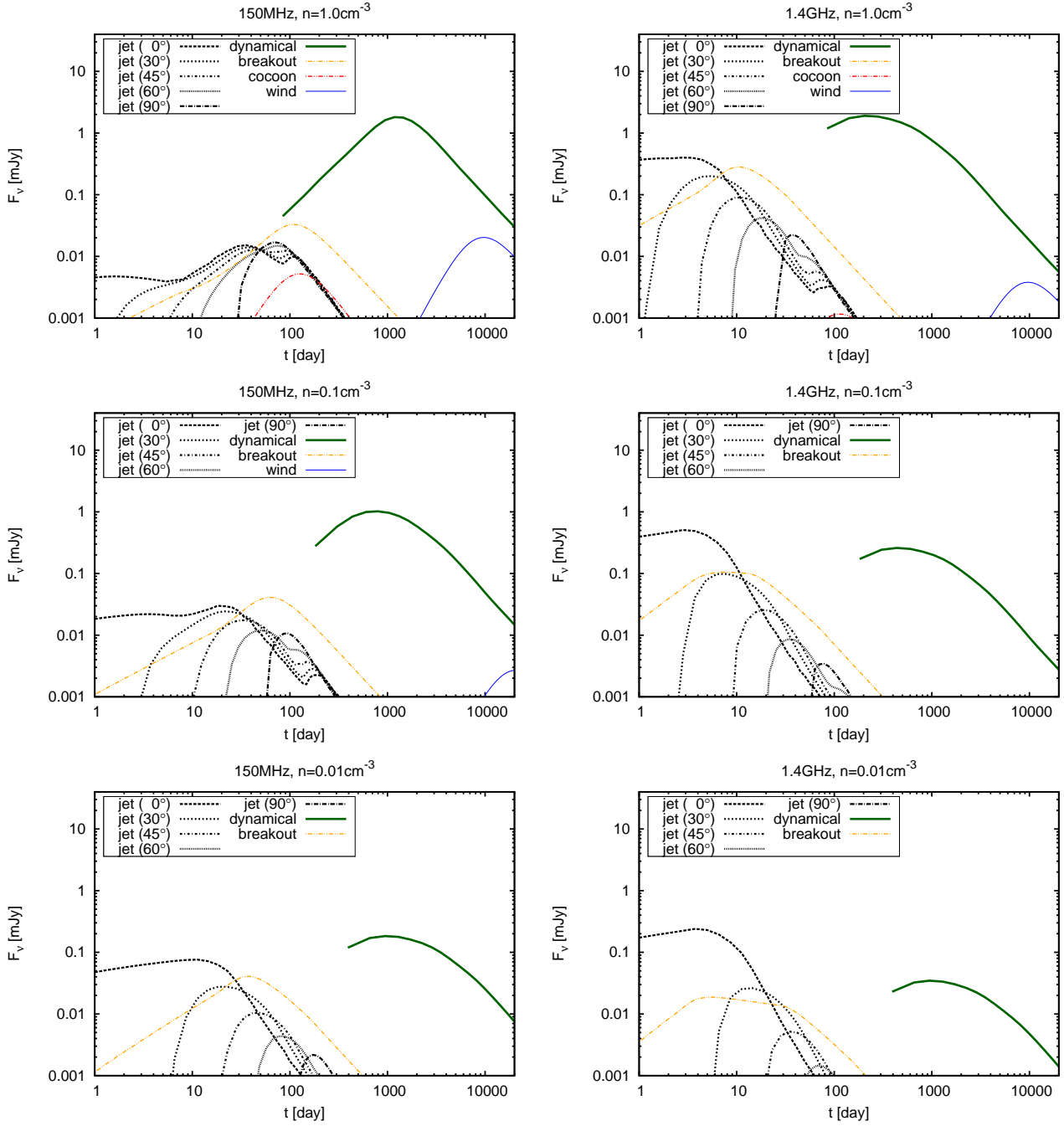


Figure 2. Radio light curves from the different ejecta components for the fiducial model. Here the energy of the ultra-relativistic jet and the cocoon is set to be 10^{48} erg and the velocity of the cocoon is $0.3c$. The external density and the luminosity distance to the source are set to be $0.01 - 1 \text{ cm}^{-3}$ and 200 Mpc. The left and right panels show the radio light curves at 150 MHz and 1.4 GHz, respectively.

low luminosity one. Figure 3 shows the radio light curves for the case of a strong GRB with a jet energy of 10^{49} erg (corresponding to an isotropic equivalent energy of $\sim 10^{51}$ erg). The energy of the cocoon is also larger as this should be comparable to the jet energy. We use $E_c = 10^{49}$ erg and a corresponding Lorentz factor of $\Gamma = 1.5$ is obtained from Eq. (1). Now, for this GRB, the on-axis GRB afterglow is the brightest at all densities at 1.4 GHz and for very low densities at 150 MHz. The cocoon is much brighter than that of the weak GRB and its peak flux at 1.4 GHz is com-

parable to that of the dynamical ejecta and to the off-axis orphan afterglow for $\theta_{\text{obs}} = 45^\circ$.

Unfortunately, there are numerous uncertainties in our estimated light curves. One of the strongest sources of the uncertainties arises from lack of precise estimates of the mass and energy of the different components. To demonstrate the possible variability of the light curves with these unknown parameters, we present in Fig. 4 the dependence of the radio flares on the kinetic energy of the different components. Here we show the light curves of the fiducial model (thick

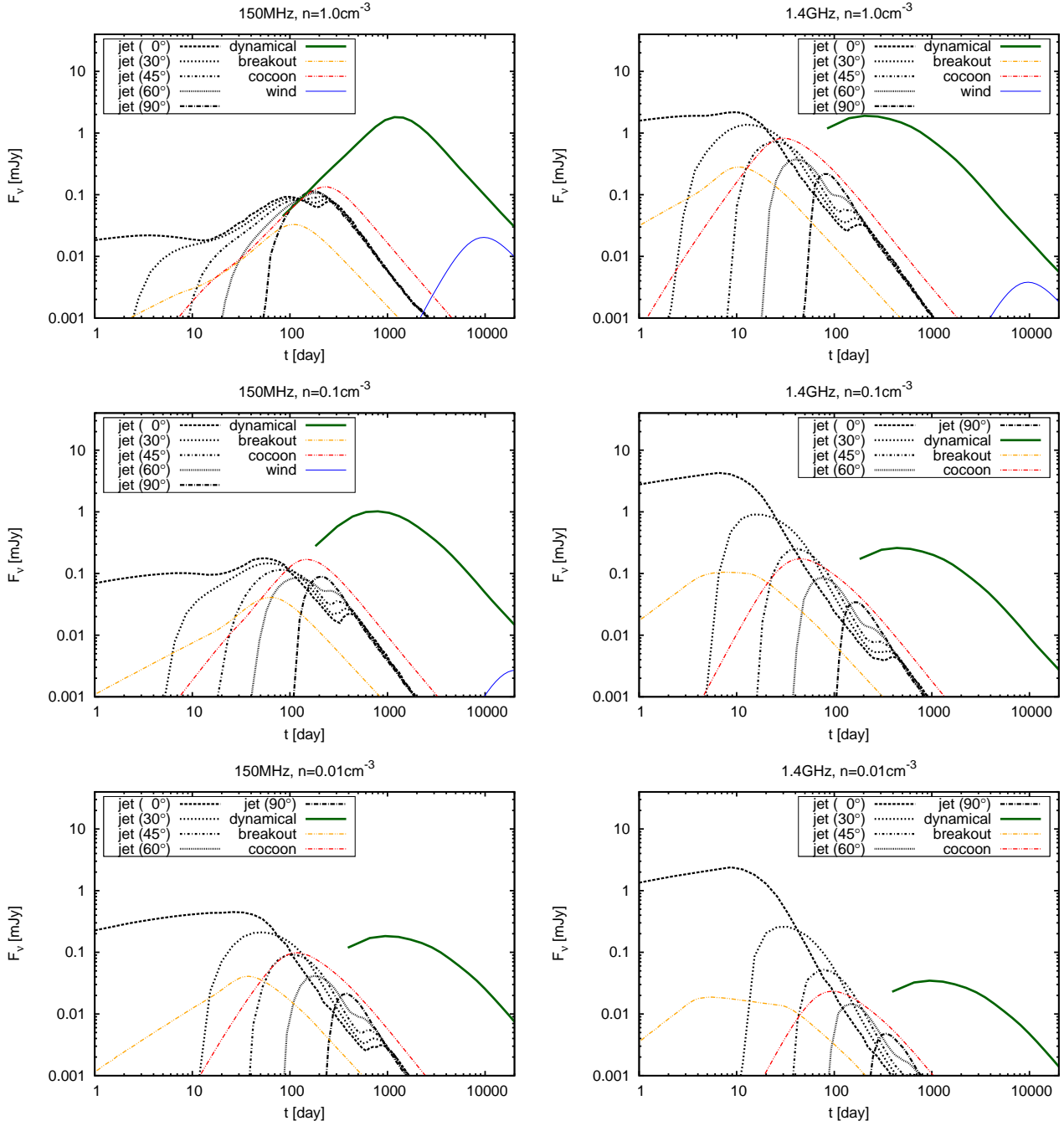


Figure 3. Same as Fig. 2 for the case of a strong GRB. The kinetic energy of the ultra-relativistic jet and the cocoon is set to be 10^{49} erg. The Lorentz factor of the cocoon is 1.5 (see Eq. 1).

curves) and those with kinetic energies larger and smaller by a factor of 3 (thin curves) than those of the fiducial model. Above (below) the self-absorption frequency, the amplitude of the light curves scales as $\propto E$ ($E^{4/5}$) and the timescale of the light curves behaves as $\propto E^{1/3}$ ($E^{5/11}$) as expected (see Sec. 3.2).

While the overall peak luminosity and peak flux depend mostly on the global properties of the outflow component, the details depend also on the spatial distribution and on the velocity distribution. For instance, the light curve of an off-axis jet rises steeply because of the collimation of the jet

and relativistic beaming effect. The detailed shapes of this rise will depend on the angular structure of the jet. The light curves of the spherical components rise slowly compared to that of off-axis afterglows. The slope of the light curve depends on the velocity distribution $E(\geq \Gamma\beta) \propto (\Gamma\beta)^{-\alpha}$. The rise of light curves will be shallower for lower values of α .

Examination of the numerical simulations reveals that the mildly and sub-relativistic components that we have examined do not satisfy indeed the spherical symmetry assumption that we have made here. Margalit & Piran (2015) have estimated the effects of a-sphericity on the emission,

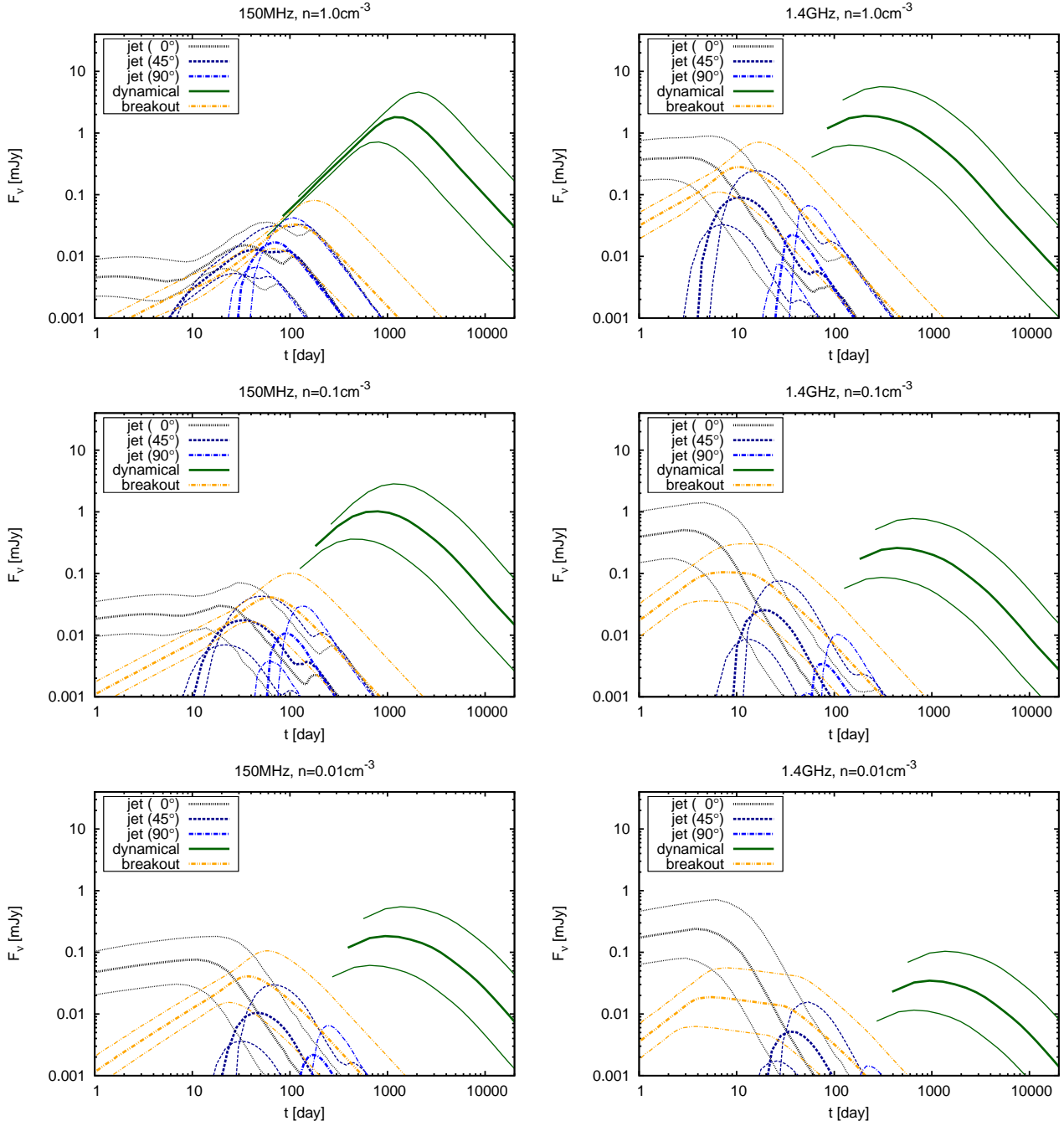


Figure 4. Uncertainties in the radio light curves. The thick lines denote the light curves of the fiducial case (see Fig. 2) and the thin curves denote the light curves with a kinetic energy larger and smaller by a factor of 3 than those of the fiducial models.

focusing on the dynamical ejecta. They found that, for a given total mass, energy, and external density, a-sphericity typically delays the peak emission and reduces the peak flux. This can be understood intuitively as follows. If more mass and energy are concentrated in one direction the matter propagating in that direction will slow down later. This longer deceleration time results in a longer and weaker radio flare compared with the isotropic one. Note that, however, as the outflow is only mildly relativistic, even from a highly a-spherical ejecta, the emission will be roughly isotropic and viewing angle effects will be small. It is worth noting that the

effect of a-sphericity is more relevant for black hole neutron star mergers, which can result in highly a-spherical mass ejection (see e.g., Kyutoku et al. 2013; Foucart et al. 2013).

4 THE RADIO SIGNATURE OF THE SHORT GRB 130603B

The short GRB 130603B had an associated macronova candidate (Berger et al. 2013; Tanvir et al. 2013). While the macronova identification is based only on one observed

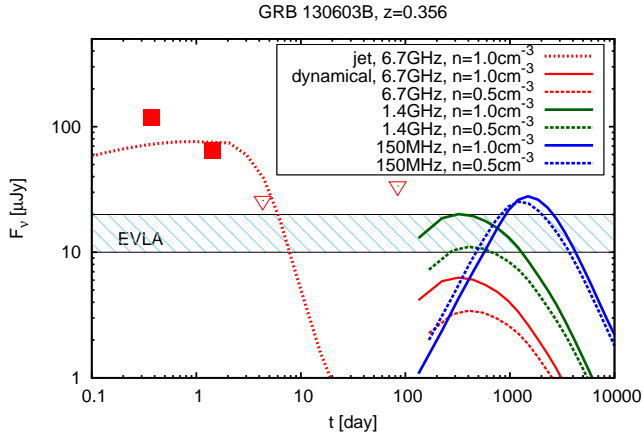


Figure 5. Radio signatures of the short GRB 130603B and light curves at 6.7 GHz (red curves), 1.4 GHz (green curves), and 150 MHz (blue curves). The red dotted curve denotes the GRB radio afterglow from a jet with $E = 8 \times 10^{48}$ erg, $\theta_j = 4^\circ$, $p = 2.3$, $\epsilon_e = 0.2$, $\epsilon_B = 8 \times 10^{-3}$, and $n = 1.0 \text{ cm}^{-3}$. The solid and dashed curves denote the expected radio light curves from a dynamical ejecta with an external density $n = 1.0 \text{ cm}^{-3}$ and 0.5 cm^{-3} , respectively. For the dynamical ejecta, the kinetic energy is assumed to be 8×10^{50} erg and the other microphysics parameters are the same as those in Sec. 3. The filled squares and the open triangles show the observed data points and the upper limits at 6.7 GHz obtained with the VLA (Fong et al. 2014). The blue shaded region shows the expected sensitivity of the EVLA at 1.4 GHz.

data point in the H -band at about 7 days (in source frame) after the burst, this is the first, even though rather weak, evidence of the significant mass ejection from a ns^2 . Using this data point, one can estimate, from the observed luminosity of the macronova, the minimal ejecta mass as $M_{\text{ej}} \approx 0.02(\epsilon_{\text{th}}/0.5) M_\odot$ (Hotokezaka et al. 2013; Piran et al. 2014), where ϵ_{th} is the conversion efficiency from the total energy generated by radioactive decay into the thermal energy of the ejecta. The velocity can be also estimated as $v \gtrsim 0.1c$ from the condition that radiation can diffuse out from the ejecta with a mass $M_{\text{ej}} \gtrsim 0.02 M_\odot$ and an opacity of $10 \text{ cm}^2/\text{g}$ (Kasen et al. 2013; Tanaka & Hotokezaka 2013) at about 7 days after the burst. Assuming that the ejecta mass and average velocity is $M_{\text{ej}} \sim 0.02 M_\odot$ and $v \sim 0.2c$, the estimated kinetic energy is about 10^{51} erg.

Figure 5 shows the expected radio flares from the dynamical ejecta at 150 MHz, 1.4 GHz, and 6.7 GHz as well as the observed early radio afterglow of GRB 130603B at 6.7 GHz by the VLA (Fong et al. 2014). Here we also show a GRB afterglow light curve which is obtained with parameters $E = 8 \times 10^{48}$ erg, $\theta_j = 4^\circ$, $p = 2.3$, $\epsilon_e = 0.2$, $\epsilon_B = 8 \times 10^{-3}$, and $n = 1.0 \text{ cm}^{-3}$. The light curve is consistent with the observed data points and upper limits⁴ within a factor of 2. It is worth emphasizing that the parameters can change by orders of magnitude and still fit the data. For instance, the external density lies in the range $n \approx 5 \times 10^{-3} -$

30 cm^{-3} (Fong et al. 2014). For modeling the radio flare from the dynamical ejecta, we assume an external density to be 1.0 and 0.5 cm^{-3} and we use an ejecta mass $M = 0.02 M_\odot$ and a kinetic energy $E = 8 \times 10^{50}$ erg. The predicted dynamical ejecta light curves at 6.7 GHz are well below the upper limits $F_\nu \lesssim 30 \mu\text{Jy}$ at ~ 80 days. However, later observations may detect a signal. Specifically the peak flux at 1.4 GHz can be as high as $F_\nu \approx 20 \mu\text{Jy}$ (depending on the external density). The expected sensitivity of the EVLA at 1.4 GHz is also shown in the figure. For the higher range of external densities $n \gtrsim 0.5 \text{ cm}^{-3}$, the radio flare might be detectable with the EVLA. The signal at 150 MHz can be $F_\nu \approx 30 \mu\text{Jy}$, which might be also detectable with the LOFAR. A positive detection of a varying radio signal will confirm the identification of this event as a ns^2 merger and will establish the observed infrared bump as a macronova.

5 CONCLUSION AND DISCUSSION

A ns^2 merger ejects a significant amount of mass in several different components: a dynamical ejecta, a shock-breakout material, a wind from a black hole/neutron star surrounded by an accretion disk, and a relativistic jet, producing a GRB. As a result of the interaction of the relativistic jet with the earlier and slower ejecta along the rotational axis, a cocoon is expected to be formed and expands nearly spherically. Among the different components of the ejecta, the dynamical ejecta, which is also the most robustly found in numerical simulations, has the largest amount of kinetic energy up to $E \sim 10^{51}$ erg. This is comparable to the “isotropic equivalent” energy of the highly beamed GRB jet. Somewhat surprisingly the beamed GRB jet is among the least energetic. Overall we have three important distinct components, the dynamical ejecta, which is mostly sub-relativistic, the mildly relativistic shock-breakout material and cocoon⁵, and the ultra-relativistic beamed jet.

We have calculated the expected radio signals produced via synchrotron emission from electrons accelerated in the shocks formed between the different components of the ejecta and the ISM. This would be a low frequency (as opposed to the X-ray or optical GRB afterglow or the optical-infrared macronova) electromagnetic counterpart of the GW event. This process is similar to GRB afterglows and radio emission of some early supernova remnants. In contrast with the high frequency counterparts, this emission lasts much longer and may even peak a few years after the merger. We focused on the expected radio flux at two frequencies of 150 MHz and 1.4 GHz. We found that there are three types of the radio flares: (i) The ultra-relativistic jet produces the earliest bright radio flare with a timescale of ~ 10 days for an observer along the jet axis or close to it. (ii) A radio flare with a timescale of a few dozen days is produced by the mildly relativistic components such as the shock-breakout material, the off-axis jet, and the cocoon. The latter flare from the cocoon is significant only when the cocoon is energetic enough so that it has a relativistic velocity. (iii) Finally the sub-relativistic dynamical ejecta

⁴ The light curve that we obtain is also consistent with the observed data in other frequencies except for the late time excess in the H -band (the macronova candidate) and in the X-ray band.

⁵ Note that the velocity of the cocoon depends on the energy deposited into the cocoon. The cocoon will be relativistic when the deposited energy is larger than about 10^{49} erg.

produces a radio flare with a timescale of a few years. At 150 MHz, however, the radio flare is strongly suppressed by synchrotron self absorption for $n \gtrsim 0.01 \text{ cm}^{-3}$ until a few months. Hence the earlier signals are much weaker at low frequencies. Depending on the external density and the distance to the source, these radio flares could be detectable as GW counterparts. Such a detection can reveal the nature of ns^2 mergers.

Although the modeling of radio emission from mergers contains uncertain parameters such as the kinetic energy of the ejecta and the external density, it is worth to estimate these values from the nature of the short GRB 130603B. The detection of a macronova candidate associated with this event allows us to estimate the ejecta mass $M_{\text{ej}} \approx 0.02(\epsilon_{\text{th}}/0.5) M_{\odot}$. Assuming the velocity of the ejecta is $0.2c$, the estimated kinetic energy is about 10^{51} erg. The detection of the afterglows implies that the external density is in the range of $n \approx 5 \times 10^{-3} - 30 \text{ cm}^{-3}$ (Fong et al. 2014). The radio afterglow of GRB 130603B, that arose from the relativistic jet, decayed quickly and it was below $30 \mu\text{Jy}$ at ~ 4 days with a similar upper limit at 80 days. However it is still possible to observe the late-long lasting radio signal arising from the dynamical ejecta. This signal could be as high as $20 \mu\text{Jy}$ at 1.4 GHz depending mostly on the external density. For the higher range of external densities $n \gtrsim 0.5 \text{ cm}^{-3}$, this would be detectable at 1.4 GHz with the EVLA. At 150 MHz, the expected flux is about $30 \mu\text{Jy}$, which depends weakly on the external density and peaks at late times. This flux might be detectable with the LOFAR. While a detection is uncertain, a positive radio signal will confirm the identification of this event as a ns^2 merger and will establish the observed infrared bump as a macronova.

ACKNOWLEDGMENTS

We thank J. Granot, E. Nakar, L. Nava, S. Nissanke, R. Sari, and R. Shen for fruitful discussions. This research was supported by an ERC advanced grant (GRBs) and by the I-CORE Program of the Planning and Budgeting Committee and The Israel Science Foundation (grant No 1829/12).

REFERENCES

- Abadie J., Abbott B. P., Abbott R., Abernathy M., Accadia T., Acernese F., Adams C., Adhikari R., Ajith P., Allen B., et al. 2010, *Classical and Quantum Gravity*, 27, 173001
- Accadia T., et al. 2011, *Classical and Quantum Gravity*, 28, 114002
- Aso Y., Michimura Y., Somiya K., Ando M., Miyakawa O., Sekiguchi T., Tatsumi D., Yamamoto H., 2013, *Phys. Rev. D.*, 88, 043007
- Barnes J., Kasen D., 2013, *ApJ*, 775, 18
- Bartos I., Veres P., Nieto D., Connaughton V., Humenysky B., Hurley K., Márka S., Mészáros P., Mukherjee R., O’Brien P., Osborne J. P., 2014, *MNRAS*, 443, 738
- Bauswein A., Goriely S., Janka H.-T., 2013, *ApJ*, 773, 78
- Berger E., Fong W., Chornock R., 2013, *ApJL*, 774, L23
- Bucciantini N., Metzger B. D., Thompson T. A., Quataert E., 2012, *MNRAS*, 419, 1537
- Chevalier R. A., 1982, *ApJ*, 258, 790
- Chevalier R. A., 1998, *ApJ*, 499, 810
- Ciolfi R., Siegel D. M., 2014, *ArXiv e-prints*
- Davies M. B., Benz W., Piran T., Thielemann F. K., 1994, *ApJ*, 431, 742
- De Colle F., Ramirez-Ruiz E., Granot J., Lopez-Camara D., 2012, *ApJ*, 751, 57
- Dessart L., Ott C. D., Burrows A., Rosswog S., Livne E., 2009, *ApJ*, 690, 1681
- Eichler D., Livio M., Piran T., Schramm D. N., 1989, *Nature*, 340, 126
- Fairhurst S., 2011, *Classical and Quantum Gravity*, 28, 105021
- Fernández R., Kasen D., Metzger B. D., Quataert E., 2015, *MNRAS*, 446, 750
- Fernández R., Metzger B. D., 2013, *MNRAS*
- Fong W., Berger E., Metzger B. D., Margutti R., Chornock R., Migliori G., Foley R. J., Zauderer B. A., Lunnan R., Laskar T., Desch S. J., Meech K. J., Sonnett S., Dickey C., Hedlund A., Harding P., 2014, *ApJ*, 780, 118
- Foucart F., Deaton M. B., Duez M. D., Kidder L. E., MacDonald I., Ott C. D., Pfeiffer H. P., Scheel M. A., Szilagyi B., Teukolsky S. A., 2013, *Phys. Rev. D.*, 87, 084006
- Frail D. A., Soderberg A. M., Kulkarni S. R., Berger E., Yost S., Fox D. W., Harrison F. A., 2005, *ApJ*, 619, 994
- Frail D. A., Waxman E., Kulkarni S. R., 2000, *ApJ*, 537, 191
- Goriely S., Bauswein A., Janka H.-T., 2011, *ApJL*, 738, L32
- Granot J., Piran T., 2012, *MNRAS*, 421, 570
- Granot J., Piran T., Sari R., 1999a, *ApJ*, 513, 679
- Granot J., Piran T., Sari R., 1999b, *ApJ*, 527, 236
- Grossman D., Korobkin O., Rosswog S., Piran T., 2014, *MNRAS*, 439, 757
- Hotokezaka K., Kiuchi K., Kyutoku K., Muranushi T., Sekiguchi Y.-i., Shibata M., Taniguchi K., 2013, *Phys. Rev. D.*, 88, 044026
- Hotokezaka K., Kiuchi K., Kyutoku K., Okawa H., Sekiguchi Y.-i., Shibata M., Taniguchi K., 2013, *Phys. Rev. D.*, 87, 024001
- Hotokezaka K., Kyutoku K., Tanaka M., Kiuchi K., Sekiguchi Y., Shibata M., Wanajo S., 2013, *ApJL*, 778, L16
- Just O., Bauswein A., Ardevol Pulpillo R., Goriely S., Janka H.-T., 2014, *ArXiv e-prints*
- Kanner J., Baker J., Blackburn L., Camp J., Mooley K., Mushotzky R., Ptak A., 2013, *ApJ*, 774, 63
- Kasen D., Badnell N. R., Barnes J., 2013, *ApJ*, 774, 25
- Kasliwal M. M., Nissanke S., 2014, *ApJL*, 789, L5
- Kisaka S., Ioka K., Takami H., 2014, *ArXiv e-prints*
- Kochanek C. S., Piran T., 1993, *ApJL*, 417, L17
- Korobkin O., Rosswog S., Arcones A., Winteler C., 2012, *MNRAS*, 426, 1940
- Kyutoku K., Ioka K., Shibata M., 2013, *Phys. Rev. D*, 88, 041503
- Kyutoku K., Ioka K., Shibata M., 2014, *MNRAS*, 437, L6
- Li L.-X., Paczyński B., 1998, *ApJL*, 507, L59
- Margalit B., Piran T., 2015, in preparation
- Metzger B. D., Bauswein A., Goriely S., Kasen D., 2015, *MNRAS*, 446, 1115
- Metzger B. D., Berger E., 2012, *ApJ*, 746, 48
- Metzger B. D., Fernández R., 2014, *MNRAS*, 441, 3444
- Metzger B. D., Martínez-Pinedo G., Darbha S., Quataert E., Arcones A., Kasen D., Thomas R., Nugent P., Panov

- I. V., Zinner N. T., 2010, MNRAS, 406, 2650
- Metzger B. D., Piro A. L., 2014, MNRAS, 439, 3916
- Murguia-Berthier A., Montes G., Ramirez-Ruiz E., De Colle F., Lee W. H., 2014, ApJL, 788, L8
- Nagakura H., Hotokezaka K., Sekiguchi Y., Shibata M., Ioka K., 2014, ApJL, 784, L28
- Nakamura T., Kashiya K., Nakauchi D., Suwa Y., Sakamoto T., Kawai N., 2014, ApJ, 796, 13
- Nakar E., 2007, Phys. Rep., 442, 166
- Nakar E., Piran T., 2011, Nature, 478, 82
- Nissanke S., Kasliwal M., Georgieva A., 2013, ApJ, 767, 124
- Nissanke S., Sievers J., Dalal N., Holz D., 2011, ApJ, 739, 99
- Oechslin R., Janka H.-T., Marek A., 2007, A&A, 467, 395
- Perego A., Rosswog S., Cabezón R. M., Korobkin O., Käppeli R., Arcones A., Liebendörfer M., 2014, MNRAS, 443, 3134
- Piran T., Korobkin O., Rosswog S., 2014, ArXiv e-prints
- Piran T., Nakar E., Rosswog S., 2013, MNRAS, 430, 2121
- Rezzolla L., Baiotti L., Giacomazzo B., Link D., Font J. A., 2010, Classical and Quantum Gravity, 27, 114105
- Rezzolla L., Kumar P., 2014, ArXiv e-prints
- Rosswog S., 2013, Royal Society of London Philosophical Transactions Series A, 371, 20272
- Rosswog S., Liebendörfer M., Thielemann F.-K., Davies M. B., Benz W., Piran T., 1999, A&A, 341, 499
- Ruffert M., Janka H.-T., Takahashi K., Schaefer G., 1997, A&A, 319, 122
- Rybicki G. B., Lightman A. P., 1979, Radiative processes in astrophysics
- Sari R., 1998, ApJL, 494, L49
- Sari R., Piran T., Narayan R., 1998, ApJL, 497, L17
- Schutz B. F., 2011, Classical and Quantum Gravity, 28, 125023
- Seto N., 2015, MNRAS, 446, 2887
- Shibata M., Taniguchi K., 2006, Phys. Rev. D., 73, 064027
- Tan J. C., Matzner C. D., McKee C. F., 2001, ApJ, 551, 946
- Tanaka M., Hotokezaka K., 2013, ApJ, 775, 113
- Tanvir N. R., Levan A. J., Fruchter A. S., Hjorth J., Hounsell R. A., Wiersema K., Tunnicliffe R. L., 2013, Nature, 500, 547
- The LIGO Scientific Collaboration 2014, ArXiv e-prints
- van Eerten H. J., MacFadyen A. I., 2011, ApJL, 733, L37
- Wanajo S., Sekiguchi Y., Nishimura N., Kiuchi K., Kyutoku K., Shibata M., 2014, ApJL, 789, L39
- Wanderman D., Piran T., 2014, ArXiv e-prints
- Zhang B., 2013, ApJL, 763, L22